Astron. Astrophys. 356, 347–356 (2000)

ASTRONOMY AND ASTROPHYSICS

Seasonal effects in the thermal structure of Saturn's stratosphere from infrared imaging at 10 microns

J.L. Ollivier[1], F. Billebaud[1], P. Drossart[2], M. Dobrijévic[1], M. Roos-Serote[3], T. August-Bernex[1], and I. Vauglin[4,*]

[1] Observatoire de Bordeaux, BP 89, 32270 Floirac, France
[2] DESPA, Observatoire de Paris, 92195 Meudon, France
[3] Observatorio Astronomico de Lisboa, 1349-018 Lisboa, Portugal
[4] Observatoire de Lyon, 69561 Saint Genis Laval, France

Received 1 October 1999 / Accepted 27 January 2000

Abstract. We present thermal infrared images of Saturn recorded with the Canada-France-Hawaii 3.6 meter Telescope (CFHT) in 1992, during Saturn's northern summer (145.5°of solar longitude). These observations were made using C10μ, a 64×64 pixel camera, at 6 different wavelengths (10.91, 11.69, 12.47, 13.09, 13.29 and 13.48 μm), sensitive to phosphine (PH_3), ethane (C_2H_6), and acetylene (C_2H_2). Many features are clearly visible, in particular (i) a bright north-equatorial belt (11.69, 12.47, 13.09, 13.29 and 13.48 μm), (ii) a very bright north-polar emission (especially at 11.69 and 12.47 μm), (iii) a darker zone corresponding to the ring occultation. We used an infrared radiative transfer code to model the emission of Saturn's atmosphere at the observed wavelengths. Three set of parameters are of importance: (i) the cloud distribution and properties, (ii) the thermal profile, and (iii) the compound abundances. From the present observations and from comparison with previous ones obtained by other authors (Tokunaga et al. 1978), we can conclude that the observed structures likely originate in the seasonal cycle of Saturn. Its effect concentrates essentially at levels located above the 200-300 mbar level. We also retrieve the latitudinal evolution of the thermal profile: we show that the tropospheric temperature decreases towards the pole by about 3K, whereas the stratospheric temperature has the same behavior as the tropospheric temperature between 15°N and 40°N, and greatly increases (about +10K) beyond 60°N. We also explore the possibility of explaining these features with variable hydrocarbon abundances: an enhancement of a factor of 5.5 of the ethane mixing ratio and of a factor of 6 of the acetylene mixing ratio appears then necessary at high latitudes (60°N). But, from comparison with previous works (Tokunaga et al. 1978), we consider that this latter explanation is not likely.

Key words: planets and satellites: individual: Saturn – infrared: solar system

Send offprint requests to: J.L. Ollivier
* Visiting Astronomer, Canada-France-Hawaii Telescope operated by the National Research Council of Canada, the Centre National de la Recherche Scientifique de France and the University of Hawaii.
Correspondence to: ollivier@observ.u-bordeaux.fr

1. Introduction

Many previous infrared observations of Saturn have led to the conclusion that a strong seasonal effect exists on Saturn in the upper atmosphere. Gillett and Orton (1975), using center-to-limb scans at 11.7 μm, showed that the south pole of Saturn was unexpectedly bright, and related this with the longer insolation of southern high latitudes, leading to a temperature enhancement. Rieke (1975) and Tokunaga et al. (1978) also observed such a feature at other wavelengths (respectively 12.35 μm and 17.8, 19.7, 22.7 μm) and derived the same conclusions. From the observations of the Voyager probes, Hanel et al. (1982) showed that the tropopause temperature is approximately 10K cooler in the north polar region than in the south polar region. Furthermore, from Voyager IRIS (Infrared Interferometer Spectrometer and Radiometer) spectra, Conrath and Pirraglia (1983) retrieved the latitudinal variations of the temperature in the troposphere at three pressure levels. Their results clearly showed a north/south asymmetry, as well as small scale thermal variations, which are assumed to be due to meridional circulation. This north/south asymmetry consists of an equator-to-pole temperature gradient which is lower towards the insolated pole than towards the pole which lies in the planetary shadow. This gradient is especially clear for the 150 mbar level (e.g. Fig. 1 of Conrath and Pirraglia, 1983), which corresponds to the upper troposphere.

Bézard et al. (1984) and Bézard & Gautier (1985) developed a seasonal climate model of Saturn's upper troposphere and stratosphere, which reproduces the strong thermal hemispheric asymmetry and its temporal evolution. They predicted a seasonal cycle with a temperature amplitude of about 30K at the 5 mbar levels of both poles, and they agreed with the observations of a warm south pole at the epoch of Voyager's observations. Moreover, they predicted a reverse situation for the following years, the north pole becoming hotter than the south pole since approximately 1985. Subsequent observations brought a confirmation: from infrared images of Saturn obtained in March 1989, Gezari et al. (1989) showed that the equator-to-north-pole temperature gradient is larger than the equator-to-south-pole gradient, confirming the presence of a seasonal effect. Conrath et al. (1990) used a radiative-dynamical code to calculate the

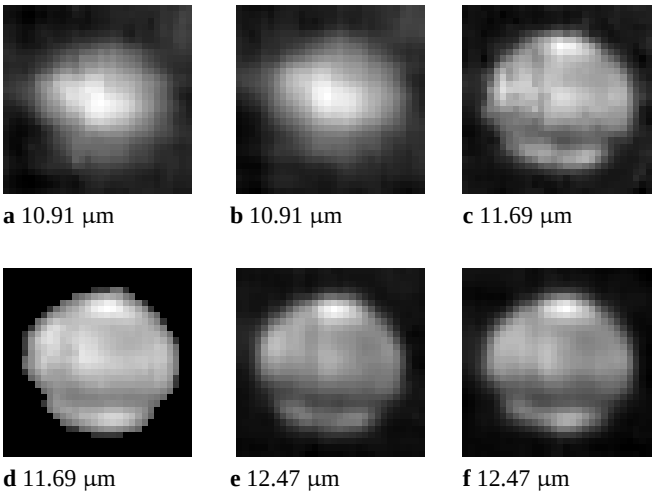

a 10.91 μm **b** 10.91 μm **c** 11.69 μm

d 11.69 μm **e** 12.47 μm **f** 12.47 μm

Fig. 1a – f. C10μ observations of Saturn on December 8, 1992.

temperatures of Saturn's atmosphere during the seasonal cycle, and Barnet et al. (1992) used an extension of the same code, but including the effects of the rings. These two models agree closely, and clearly showed the evolution of the atmosphere. In particular, the atmosphere at north summer solstice (90°of solar longitude) shows a structure which could explain quite well the observations of Gezari et al. (1989), which were obtained just after the north summer solstice, when the solar longitude of Saturn was 103.5°.

In this paper, we present observations of Saturn made with the ground-based mid-infrared camera "C10μ" at six different wavelengths (10.91, 11.69, 12.47, 13.09, 13.29, and 13.48 μm), in the thermal continuum and in the ν_9 ethane and ν_5 acetylene-band emissions. The emission of the atmosphere at these wavelengths is calculated with a line-by-line radiative transfer code and then compared with the observed fluxes. This will allow us to put constraints either on the temperature or on the hydrocarbon abundances. Ethane (C_2H_6) and acetylene (C_2H_2) are formed in the stratosphere of Saturn following methane (CH_4) photodissociation by ultraviolet photons. Their abundances have been constrained by many observations, such as Voyager's IRIS (Courtin et al. 1984) and ISO (Infrared Space Observatory, de Graauw et al. 1997) spectra. However, these observations both present limitations. As the field of view of the ISO-SWS (Short-Wavelength Spectrometer) instrument was comparable to the size of Saturn, we only have a globally-averaged value of ethane and acetylene abundances. Regarding Voyager's abundance determinations, Courtin et al. (1984) only considered a limited latitudinal range. Accordingly, no information about the spatial variations of hydrocarbon abundances is available. It is yet likely that such variations occur in giant planets' atmospheres. Indeed, hydrocarbon abundances depend on many parameters, as shown by different photochemical models (see for example Atreya, 1986, Ollivier et al. 2000a): solar insolation, temperature profile, vertical transport... Moreover, a process like the energetic particle precipitation around the poles can produce an additional chemistry which can lead to a modification of compound abundances (Kostiuk et al. 1987). Beside these possible abundance effects, the large tilt of the spin axis should produce an evolution of the thermal structure of Saturn's atmosphere, as stated by previous works (Tokunaga et al. 1978, Gillett & Orton, 1975). Nevertheless, these previous works never consider the possible variation of hydrocarbon abundances. Consequently, we will consider two assumptions in the present analysis:

- the first one considers the same ethane and acetylene abundances over all latitudes. The observed variations of the infrared flux are then only "thermal".
- the second one includes the possibility of variations of the hydrocarbon abundances.

Section 2 presents the general characteristics of the observations. Section 3 is devoted to the data reduction and calibration procedures and presents the resulting images. In Sect. 4, we describe the radiative transfer code we used and the starting hypotheses. Then, Sect. 5 is devoted to the analysis of the images and Sect. 6 to the discussion of our results.

2. Observations

The images were recorded in the 10 μm atmospheric window at the Canada-France-Hawaii Telescope on December 8, 1992, between 3^h UT and 4^h UT, and on December 9, 1992, between 2^h45 UT ans 4^h15 UT. We used "C10μ", a 64×64 pixel camera which was developed by the Equipe Infrarouge of the Observatoire de Lyon, France (Vauglin et al. 1999). The spatial sampling is 0.7 arcsec per pixel. The size of Saturn was of about 16 arcsec on December 1992, the entire planet is then visible on the camera. This camera is sensitive in the 5 to 17 μm range and we chose 6 wavelengths on a CVF (Circular Variable Filter) filter, having spectral resolution of 50. The first selected wavelength probes the thermal continuum, at 10.91 μm. Owing to the low spectral resolution, this spectral interval is also slightly sensitive to the phosphine emission. The following wavelengths, 11.69 μm and 12.47 μm, are in the wings of the ν_9 ethane band. The three last wavelengths, 13.09, 13.29 μm and 13.48 μm, correspond to the ν_5 acetylene band emission. In order to calibrate the images, we also observed at all wavelengths the standard stars β*Peg* and μ*Ceph*, whose infrared fluxes have been measured by IRAS (Infrared Astronomical Satellite, Olnon et al. 1986).

3. Data reduction

The details of the data reduction are the same as in Billebaud et al. (1995) who used the same camera and wavelength ranges to observe Jupiter. Because of the background emission of the sky and instruments at these wavelengths, observing techniques specific to thermal infared are compulsory. On December 8, we used a "chopping" mode, which substracts the contribution of the sky, and on December 9, we used a "chopping+nodding" mode, which substracts the contribution of the sky and corrects the images for the inhomogeneities of the primary mirror. The resulting images are then flat-fielded and false pixels are corrected. Integration time for an individual image is very short

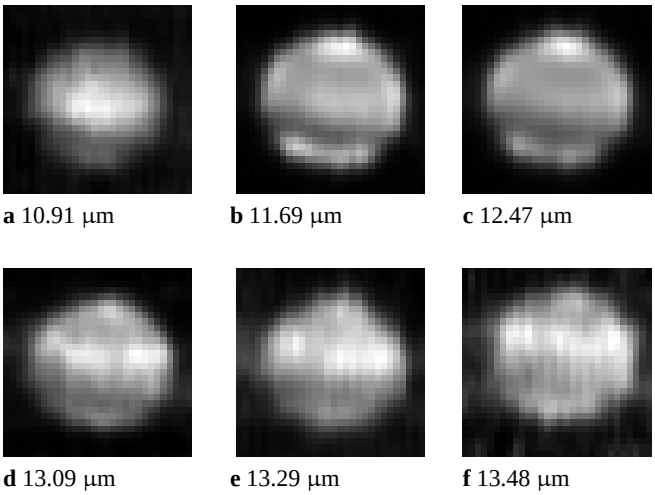

a 10.91 μm **b** 11.69 μm **c** 12.47 μm

d 13.09 μm **e** 13.29 μm **f** 13.48 μm

Fig. 2a – f. C10μ observations of Saturn on December 9, 1992.

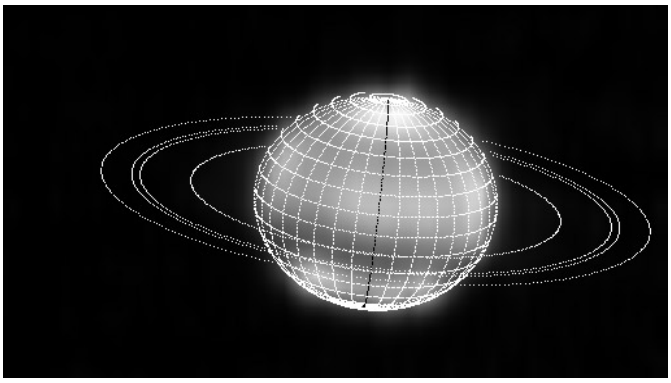

Fig. 3. Saturn at 11.69 μm the 9 December 1992. We have drawn the meridians and the parallels every 10°. The black meridian corresponds to the central one. The position of the rings is also indicated (A ring, Cassini division, and B ring).

(about 40 ms). It is also possible to add those images which are not separated by more than about 10 minutes, in order to improve the signal-to-noise ratio without degrading the spatial resolution. The deconvolution procedure uses the calibration star images to determine the Point Spread Function (PSF) of the instrument.

The December 8 images are also corrected of a background flux which is not removed by the standard procedure. It is thought to be due to the technique used to make the observations: on December 8, we made the observations without the "nodding" mode. The inhomogeneities of the primary mirror are thus not eliminated. In order to remove this contribution, we make an estimation of the averaged background flux and remove it from the images. Due to bad atmospheric conditions, the absolute calibration is not reliable for the December 8 images. Nevertheless, these images can be used to study the numerous features visible on Saturn and the relative variations of the flux. For their part, the December 9 images are of very good quality, except for the images in the acetylene band, for which the flat-fielding procedure did not remove all the instrumental line-shaped features: some groups of pixel raws of the mosaic show an additional flux. This flux is clearly visible outside the planet, but should also be present on the planet. As we will see later, these "line-shaped features" certainly affect the latitudinal variations of the flux in the acetylene band, especially at 13.29 and 13.48 μm. We use the two star β*Peg* and μ*Ceph* to calibrate the images. Finally, this gives us two sets of 6 images, one for each night. We have two images at 10.91 μm, two at 11.69 μm and two at 12.47 μm for December the $8^{\rm th}$. And for December the $9^{\rm th}$, we have one at each wavelength (10.91, 11.69, 12.47, 13.09, 13.29 and 13.48 μm). The signal-to-noise ratio depends on the date of the observations and on the wavelengths. The best signal-to-noise ratio is obtained in the ethane band emission for the December 9 images (>100) and it decreases with longer wavelengths ($\sim$ 40 at 13.09 μm, $\sim$ 10 at 13.29 μm and <10 at 13.48 μm, for the December 9 images), as well as for the 10.91 μm image ($\sim$ 8). The signal-to-noise ratio is quite low in the acetylene band because these wavelengths are at the edge of the atmospheric window, very sensitive to weather conditions. Regarding the December 8 images, the signal-to-noise ratio is lower in the ethane band ($\sim$ 20) and, at 10.91 μm, has the same order of magnitude as in the December 9 image. Fig. 1 and 2 present the images of Saturn at all wavelengths for December 8 and 9.

Geometry

The next step is to retrieve the geometry of Saturn and to associate each pixel to a latitude and longitude. First, we transform the 64×64 pixel images to 1024×1024 pixel images by making an interpolation. This leads to a better sampling and a more precise determination of the coordinates of each pixel. Then we localize the position of the center and adjust a circle on the planet. Next we make a deprojection of each pixel in the circle: first of all, we assign to each pixel a *(y,z)* coordinate (the plane corresponding to $x = 0$ corresponds to the plane of the image). Then, we retrieve the *x* coordinate: $x = \sqrt{R^2 - y^2 - z^2}$, where R is the Saturnian radius determined when drawing the circle. We also take the oblate shape of Saturn into account. Afterwards we make two rotations of the axes to take the tilt of the Saturnian spin axis into account. We can thus associate each set of coordinate *(x,y,z)* to a longitude and latitude. From planetary ephemerides, we also determine the position of the central meridian at the time of observations, and we relate each pixel to a system III longitude. Moreover, we determine the position of the rings by using a reverse procedure (from the theoretical position of the rings, we determine the (y,z) coordinates of the ring edges on our images). Fig. 3 presents a map of Saturn at 11.69 μm on December 8 with the limits of the A and B rings.

4. Radiative transfer treatment

The outgoing infrared flux is calculated with a line-by-line radiative transfer code which was primarily developed for the analysis of Galileo/NIMS data of Jupiter (see for example Roos-Serote et al. 1998) and adapted to Saturn. We only consider

the opacities of phosphine, ethane and acetylene, which are the only compounds having significant opacities in the wavelength range we study. The molecular spectroscopic parameters for PH_3, C_2H_2 and C_2H_6 are taken from the GEISA databank (Jacquinet-Husson et al. 1998). This code also includes the Collision Induced Absorption (CIA) due to H_2-H_2 and H_2-He collision (Borysow et al. 1985).

Parameters

We present here the characteristics of the thermal profile, phosphine, ethane and acetylene abundances, and cloud structure we used in our models. The determination of these parameters have generally been done only for a precise location and temporal variations certainly affect them. We then just consider the previously observed values as a starting point, the aim of our work being to give information on the variations of these parameters.

– *Thermal profile*
We use the profile derived by Lindal et al. (1985) from the radio occultation of Voyager by Saturn's atmosphere at a latitude of 36.5°N. This profile extends from 1300 mbars to 0.2 mbar and shows a tropopause temperature of 82K. Hubbard et al. (1997) determined the thermal structure of Saturn's mesosphere, above the profile derived by Lindal et al. (1985), from the occultation of *δSco*. This observation was made at near-infrared wavelengths and probed equatorial latitudes. They showed that the mesosphere of Saturn is nearly isothermal (between 140 and 150K). We construct our standard temperature profile, quoted $T_0(z)$ in the following, from these two observations: the lower part consists in the profile of Lindal et al. (1985) and the upper part (above 1 mbar) is isothermal (141K).
– *Abundances*
From the analysis of the Voyager IRIS spectra acquired in August 1981, Courtin et al. (1984) derived mixing ratios of phosphine, ethane and acetylene equal to $1.4\pm0.8\times10^{-6}$, $3\pm1.1\times10^{-6}$ and $2.1\pm1.4\times10^{-7}$ respectively, with the following vertical distributions: C_2H_6 and C_2H_2 have constant mixing ratios above 20-50mbar, and PH_3 has a constant mixing ratio below 3-6 mbar. These results were derived from spectra probing northern latitudes (20°-40°N), around the location of the Voyager 2 ingress temperature profile (36.5°N). Phosphine is present only in the lower part of the atmosphere of Saturn (Courtin et al. 1984), below levels around 3-6 mbar, therefore, its mixing ratio at higher altitudes is set to zero. Ethane and acetylene, for their part, are produced in the stratosphere and then transported to upper and lower levels. Photochemical models calculate the vertical distribution of such compounds and show that their mixing ratios are not constant with altitudes (Strobel 1983, Gladstone et al. 1996, Moses et al. 1999, Ollivier et al. 2000a). Therefore the vertical distribution of ethane and acetylene is an additional parameter. In order to obtain the vertical distribution of C_2H_2 and C_2H_6, we use an improved version of the model of Ollivier et al. (2000a). Their results show a discrepancy between the calculated ethane mole fraction and the values derived from the observations of Voyager/IRIS or ISO/SWS. Some corrections of the chemical scheme have been done and with an adequate eddy diffusion coefficient profile, a good agreement between the observed and calculated ethane and acetylene mole fraction is obtained (a detailed explanation of the corrections will be available in Ollivier et al. 2000b). Fig. 4 presents the resulting ethane and acetylene mole fraction vertical profile, which we use in our radiative transfer calculations. The vertical distribution of the molecules is then not anymore a parameter.

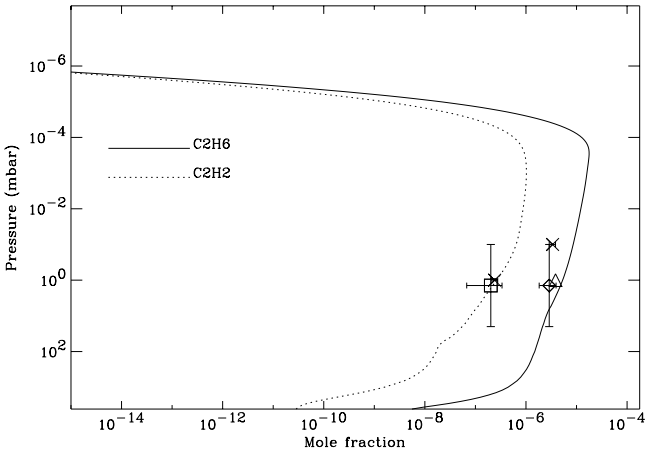

Fig. 4. Vertical distribution of ethane and acetylene mole fraction. These distributions are the same as in Ollivier et al. (2000b), where one can find the values of the different parameters used to calculate these profiles. The results of different observations are presented. The diamond and the square correspond respectively to the ethane and acetylene mole fraction derived by Courtin et al. (1984) from Voyager/IRIS spectra. The triangle is the value of ethane mole fraction retrieved from ISO spectra (de Graauw et al. 1997) and the two crosses represent two values of acetylene mole fraction derived by de Graauw et al. (1997) for two different altitudes.

– *Cloud structure*
The cloud structure is the less constrained parameter. Many studies of Saturn's clouds have been made from visible images, but their optical properties in the infrared are not well known. In order to fit the ISO spectra, de Graauw et al. (1997) had to include some clouds in their radiative transfer model. They considered two cloud layers: the first cloud is located at a pressure of 1.55 bar and has a transmission of 0.2, and the second cloud, at 0.55 bar, has a transmission 0.9. In our analysis, we considered the same structure without any spatial variations and the clouds are supposed to be grey absorbers.

5. Analysis

5.1. Qualitative analysis

The most prominent feature visible on Saturn's disk, especially in the ethane band, is the north-polar emission (NPE). It is located above 50°N and it seems to extend all around the pole.

Table 1. The characteristics of the different observations of Saturn. L_s refers to the solar longitude. The seasons correspond to those of the northern hemisphere. The last column indicates the main feature seen on the corresponding observation.

Ref.	Date	L_s	Wavelength (μm)	Season	Observed features
Gillett & Orton (1975)	9/1973	273°	11.7 μm	winter solstice	bright South Pole
Rieke (1975)	3/1974	280°	12.35 μm	early winter	bright South Pole
Tokunaga et al. (1978)	2/1975	292.5°	17.8, 19.7 and 22.7 μm	winter	bright South Pole
Tokunaga et al. (1978)	3/1977	321°	17.8, 19.7 and 22.7 μm	winter	bright South Pole
Conrath & Pirraglia (1983)	8/1981	18°	16.5-50 μm	early spring	bright South Pole
Gezari et al. (1989)	3/1989	103.5°	7.8, 11.6 and 12.4 μm	early summer	bright North Pole
this work	12/1992	145.5°	10.91 μm	late summer	no structure
this work	12/1992	145.5°	11.69, 12.47, 13.09, 13.29, 13.48 μm	late summer	bright North Pole

Due to the geometry of Saturn, we cannot see if the NPE is centered on the north pole, but it is likely that it is present at all longitudes. The NPE has also been observed by Gezari et al. (1989) on images recorded in March 1989 at 7.8, 11.6 and 12.4 μm. Unlike these two recent observations, Gillett and Orton (1975), Rieke (1975) and Tokunaga et al. (1978) (see Table 1 for the characteristics of the different observations considered here) pointed out from infrared observations that the south pole of Saturn was very bright. The geometry of Saturn during these latter observations was the opposite of ours, and their south-polar emission was related to the greater insolation time of the south pole at the time of their observations. Thus we conclude that a greater insolation time tends to increase the temperature of the insolated pole, but with a phase lag due to the inertia of the atmospheric response (Fig. 2 of Conrath & Pirraglia, 1983). Indeed, this is clear from Table 1, where we see that Voyager observations showed a warm south pole during early northern spring. It must be noticed that limb-brightening also contributes to the enhanced emission at the pole: for instance, at 12.47 μm, the flux for a viewing angle of 80°is 41% greater than for 0°. Nevertheless, this is not enough to explain the observed features and in the next section, we will show that this feature could be due to an enhancement of the hydrocarbon abundances or a hotter stratosphere.

As noticeable as the NPE is the north-equatorial belt (NEB). This structure is also visible at all wavelengths, except at 10.91 μm where it is less evident, and is located all around the planet between 10°and 30°N, its area varying with the longitude and wavelength. Its maximum is located around 20°N. This feature can be associated with the thermal structure of the atmosphere. Indeed, from Voyager/IRIS spectra, Conrath and Pirraglia (1983) retrieved the latitudinal temperature variations at three pressure levels. In their Fig. 1, we see a strong increase of the temperature at the 150 mbar level between 10° and 20° in both hemispheres. We logically assume that these thermal structures are not confined to a pressure level around 150 mbar and extend to levels sounded on our images, which are located between 100 and 500 mbars (Table 2), and therefore are associated with the NEB.

The dark structure south of the equator is due to the rings. The observations of Voyager 2 indicated that the rings' opacity in the infrared is important, especially that of the B ring (Hanel et al. 1982). Moreover, the rings are colder than Saturn's upper troposphere and thus they would appear in absorption at 10 microns. Another effect, which we did not study, is the cooling of the part of the atmosphere which lies in the shadow of the rings (see Barnet et al. (1992) which have included the different effects of the rings in a radiative-dynamical model to study the thermal structure of the Saturnian atmosphere).

Table 2. Pressure levels (in mbar) of the maxima of the contribution function. Except for 10.91 μm, there is a maximum of the contribution function in the troposphere (Tropo.) and in the stratosphere (Strato.). These pressure levels have been determined for two different viewing angles, 0°and 70°. The sixth column indicates the corresponding molecular band.

Wavelength (μm)	Pressure level (mbar)				Molecular band
	0°		70°		
	Tropo.	Strato.	Tropo.	Strato.	
10.91	540		300		
11.69	480	2	230	2	C_2H_6 ν_9
12.47	370	2	180	2	C_2H_6 ν_9
13.09	290	3	160	3	C_2H_2 ν_5
13.29	270	4	160	4	C_2H_2 ν_5
13.48	230	4	130	3	C_2H_2 ν_5

Many other features are visible on Saturn, especially on the NEB. These small-scale structures are not well defined and it is difficult to identify them from one image to another. For instance, on the images of December 8, at 11.69 μm, a bright spot seems to be present at a longitude of 160°. This longitude range is visible on the second image of December 8, but unfortunately not on the December 9 images. Such a bright spot is also visible on the former, at a longitude of 150°. The imprecision on the geometry of Saturn could have led to a difference of 10°on the longitude, but we cannot be sure that it is the same structure we see on the two images. These possible features could be associated with temperature variations or changes in the cloud structure.

5.2. Quantitative analysis

Due to their lower quality, we do not study the December 8 images. Nevertheless, the observed stuctures are almost the same on the two sets of images. In this work, we only study the latitu-

dinal variations of the infrared flux, and we limit ourselves to the northern hemisphere. Indeed, we have a well-defined latitudinal structure (10°N-30°N: the north-equatorial belt, 30°N-50°N: a darker region, and above 50°N: the north-polar emission) at nearly all longitudes. We do not study the southern hemisphere because of the less favourable geometry and the ring occultation. We also restrict our analysis to the central meridian: it corresponds to a longitude around 240° for the December 9 images at 10.91, 11.69 and 12.47 μm, and around 275° for the December 9 images in the acetylene band (all the latitudinal structures are visible on the central meridian). The purpose of this analysis is to reproduce the observed variations of the infrared fluxes at all wavelengths. We choose to calculate the flux for five different viewing angles: 0°, 15°, 30°, 40°and 50°. Since the planetocentric latitude of the sub-Earth point is equal to 17°N (exactly 16.7°N)at the time of our observations, these viewing angles correspond to planetocentric latitudes equal to 17°N, 32°N, 42°N, 52°N and 62°N. The location of the peak flux at 10.91, 11.69 and 12.47 μm occurs around 15°N in the NEB (Fig. 6 and 7). Therefore, on these images, a viewing geometry of 0°also approximately corresponds to the maximum of the NEB. At 13.09 and 13.29 μm, the maximum of the NEB is located around 20°N, and around 30°N at 13.48 μm. A possible interpretation is that the thermal structure of Saturn's atmosphere or hydrocarbon abundances shows an evolution with the latitude. But, we have seen that the images at 13.09, 13.29 and 13.48 μm are affected by an additional noise which affects some sets of pixel raws, and, in particular, one of this line-shaped features affects the signal on the NEB. Moreover, the signal-to-noise ratio is quite low for these images which are thus more sensitive to this line-shaped features than the other images. The maximum of the contribution function (Table 2) at 13.29 and 13.48 μm are very close, and it would be difficult to reproduce the observed relative variations of the flux at 13.29 and 13.48 μm with a realistic thermal profile or realistic abundance variations. Therefore we interpret the differences in the location of the maximum of the NEB as due to noise rather than being a real structure of the atmosphere. Finally, the quantitative analysis will essentially focus on the images at 10.91, 11.69, 12.47 and 13.09 μm, which show the best signal-to-noise ratio and are not affected by the additional noise. Fig. 6 and 7 present the comparison between the observed and calculated latitudinal relative variations, and we see that we obtain very good results at 10.91, 11.69, 12.47 and 13.09 μm, while no fit at 13.29 and 13.48 μm is obtained.

The contribution functions show a different behaviour for the different studied wavelengths. At 10.91 μm, the emission is centered in the thermal continuun. Owing to the low spectral resolution, this wavelength range is also sensitive to phosphine, but its contribution is very small and does not influence the outgoing flux. The maximum of the contribution function at 10.91 μm (Table 2) is located in the troposphere near 540 mbar. The image at this wavelength helps us to constrain the tropospheric temperature, since it is independant of ethane and acetylene abundances (we consider the phosphine mixing ratio as constant). At all the other wavelengths, the contribution functions have two maxima: one in the troposphere and another one in the stratosphere. These wavelengths are thus sensitive to the abundances of hydrocarbons as well as to the stratospheric temperature. Therefore a constraint is missing: with the images at 10.91 μm, we have a constraint on the tropospheric temperature, but the stratospheric temperature is unknown. We then choose to consider two different hypotheses. The analysis of previous observations of Saturn's atmosphere in the infrared always considered that the hydrocarbon abundances were constant and attributed the observed structures to thermal effects. Thus, our first hypothesis states that acetylene and ethane have the same abundance at all latitudes and that the observed features are only due to variations of the temperature profile: the resulting temperature profile is then defined by $T_0(z) + \Delta T(z)$, where $\Delta T(z)$ varies with the altitude z. The second hypothesis states that the shape of the thermal profile is constant, i.e. the temperature profile is shifted by the same values at all altitude levels: $T_0(z) + \Delta T$, where ΔT does not vary with altitude. ΔT is determined to obtain a fit with the 10.91 μm images, and the observed variations of the infrared flux are then due to variations of ethane and acetylene abundances. Table 3 displays the parameters used to calculate the flux at each latitude in the two cases.

First of all, we have explored the possibility that the cloud structure is at the origin of the observed structures. We have made some tests with different cloud distributions: they clearly show that a cloud located in the lower stratosphere could produce a quite different thermal infrared flux. The point is that it has the same effect at all wavelengths, in particular at 10.91 μm. Therefore, if the NPE was due to a different cloud distribution, it would also have been observed at 10.91 μm (if we suppose that the infrared properties of the clouds are the same at all the wavelengths concerned here). Therefore, a different cloud structure or composition cannot be at the origin of the observed structure.

5.2.1. Thermal structure vs. latitudes

In the case of constant ethane and acetylene abundances, the agreement between the variations of the observed and the calculated flux is obtained with the temperature profiles shown in Fig. 5. Fig. 6 presents the relative variations of the observed flux with latitude and the diamonds show the calculated variations obtained with the thermal profile corresponding to each latitude. At 17°N, the thermal profile $T_1(z)$ has the same shape as the standard profile but the temperatures are increased by $\Delta T(z) = 7K$ at all altitudes z: $T_1(z) = T_0(z) + 7K$. This profile leads to a good agreement with the absolute flux at 10.91 μm, but not at other wavelengths. We did not try to find an exact fit with other wavelengths because in this case, the fluxes depend on two parameters (temperature and abundances), while at 10.91 μm, the flux depends only on the thermal profile. Moreover, the calibration procedure leads to fluxes which are of the order of magnitude of the computed one, but there is some evidence for large absolute calibration uncertainties. Nevertheless, we only study the relative variations and we did not try to find an

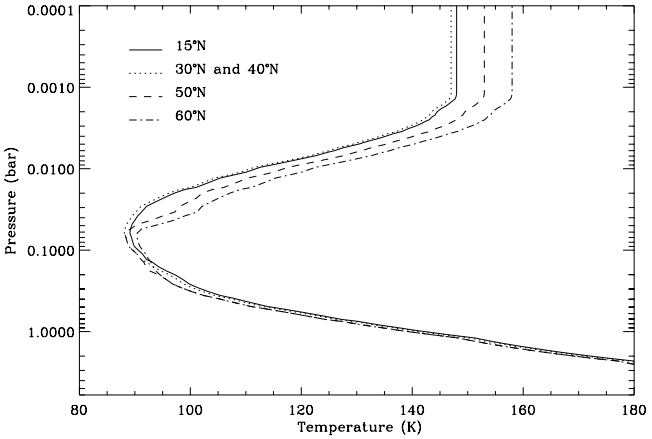

Fig. 5. The different temperature profiles used in the radiative transfer model. The solid line corresponds to the standard profile constructed from Lindal et al. (1985) and Hubbard et al. (1997), increased by 7K ($T_0(z)+7K$). This profile is used to model the flux at 15°N. The dotted line is the standard profile, increased by $\Delta T(z) = +6K$, and corresponds to 30°N. The thermal profile at 40°N is almost the same as the dotted line profile ($\Delta T(z) = +5.5K$). The dashed line shows a tropospheric temperature increased by $\Delta T(z < z_{tropopause}) = +4.5K$ and a stratospheric temperature increased by $\Delta T(z > z_{tropopause}) = +12K$ (50°N). The dash-dot line has the same tropospheric temperature as the latter and the stratospheric temperature is increased by $\Delta T(z > z_{tropopause}) = +17K$ relative to the standard one.

exact fit with the absolute flux. Consequently, we do not retrieve here any absolute parameter, such as the temperature at a given level, but we only give the relative variations of temperature (and abundances in Sect. 5.2.2.).

From the comparison between the relative variations of the observed and computed fluxes, we retrieve the latitudinal variation of the thermal profile. Between 17°N and 32°N, the temperature decreases at all levels by 1K ($T_1(z) - 1K$). Then, at 42°N, the profile is 0.5K cooler than at 32°N. At 52°N, the fit is obtained with temperatures decreased by 1.5K relative to 42°N at all levels below the tropopause ($T_1(z < z_{tropopause}) - 3K$), while the stratospheric temperatures increase by 6.5K relative to the 42°N at all altitudes ($T_1(z > z_{tropopause}) + 5K$). At 62°N, the tropospheric temperatures are the same as at 52°N, and the stratospheric ones increase again (+5K at all levels above the tropopause with respect to the 52°N profile: $T_1(z > z_{tropopause}) + 10K$). The amplitude of the latitudinal variation of the stratospheric temperature is thus about 12K at a given altitude in the stratosphere whereas that of the tropospheric temperature is about 3K.

5.2.2. Ethane and acetylene abundances

We now consider that the shape of the thermal profile is the same at all latitudes (ΔT constant with the altitude). The 10.91 μm flux is independant of the abundances of ethane and acetylene and allows us to retrieve the tropospheric temperature. Then the hypothesis of a constant temperature profile shape constrains the stratospheric temperature. The variations of the flux are then reproduced with variations of ethane and acetylene abundances. We have seen in the previous section that between 17°N and 42°N, the shift of the temperature is the same in the troposphere and in the stratosphere. The temperature profile has thus the same shape in between these latitudes, and the abundances of ethane and acetylene are constant. At 52°N, we obtain a good fit with a thermal profile decreased at all altitudes by 1K relative to 42°N ($T_1(z) - 2.5K$), and with abundances of ethane and acetylene respectively multiplied by 2.5 and 3 with respect to the calculated abundances. At 62°N, the thermal profile is the same as at 52°N, and the abundances of ethane and acetylene are multiplied by respectively 5.5 and 6 with respect to the calculated abundances. Fig. 7 shows the relative variations of the flux at all wavelengths and the computed variations.

Table 3. Parameters used to model the radiative transfer at the different latitudes. *Variable temperature & Constant abundances* refers to hypothesis 1 (we fix the ethane and acetylene mole fraction and the thermal profile varies), and *Variable abundances & Constant shape* to hypothesis two (the shape of the thermal profile is constant and ethane and acetylene abundances vary). The abundance of C_2H_6 and C_2H_2 correspond to the mole fraction profile of Fig. 4, multiplied by the indicated factor. The indicated temperature corresponds to the variation with respect to the standard profile constructed from the observations of Lindal et al. (1985) and Hubbard et al. (1997).

		Variable temperature & Constant abundances	Variable abundances & Constant shape
17°N	C_2H_6 abundance	×1	×1
	C_2H_2 abundance	×1	×1
	Tropospheric ΔT	+7K	+7K
	Stratospheric ΔT	+7K	+7K
32°N	C_2H_6 abundance	×1	×1
	C_2H_2 abundance	×1	×1
	Tropospheric ΔT	+6K	+6K
	Stratospheric ΔT	+6K	+6K
42°N	C_2H_6 abundance	×1	×1
	C_2H_2 abundance	×1	×1
	Tropospheric ΔT	+5.5K	+5.5K
	Stratospheric ΔT	+5.5K	+5.5K
52°N	C_2H_6 abundance	×1	×2.5
	C_2H_2 abundance	×1	×3
	Tropospheric ΔT	+4K	+4.5K
	Stratospheric ΔT	+12K	+4.5K
62°N	C_2H_6 abundance	×1	×5.5
	C_2H_2 abundance	×1	×6
	Tropospheric ΔT	+4K	+4.5K
	Stratospheric ΔT	+17K	+4.5K

6. Discussion

In the following, we compare our results with previous infrared observations of Saturn (Gezari et al. 1989, Tokunaga et al. 1978). These observations have been obtained at several wavelengths, different or not from ours, and give additional constraints on the analysis of thermal structure and hydrocarbon abundances

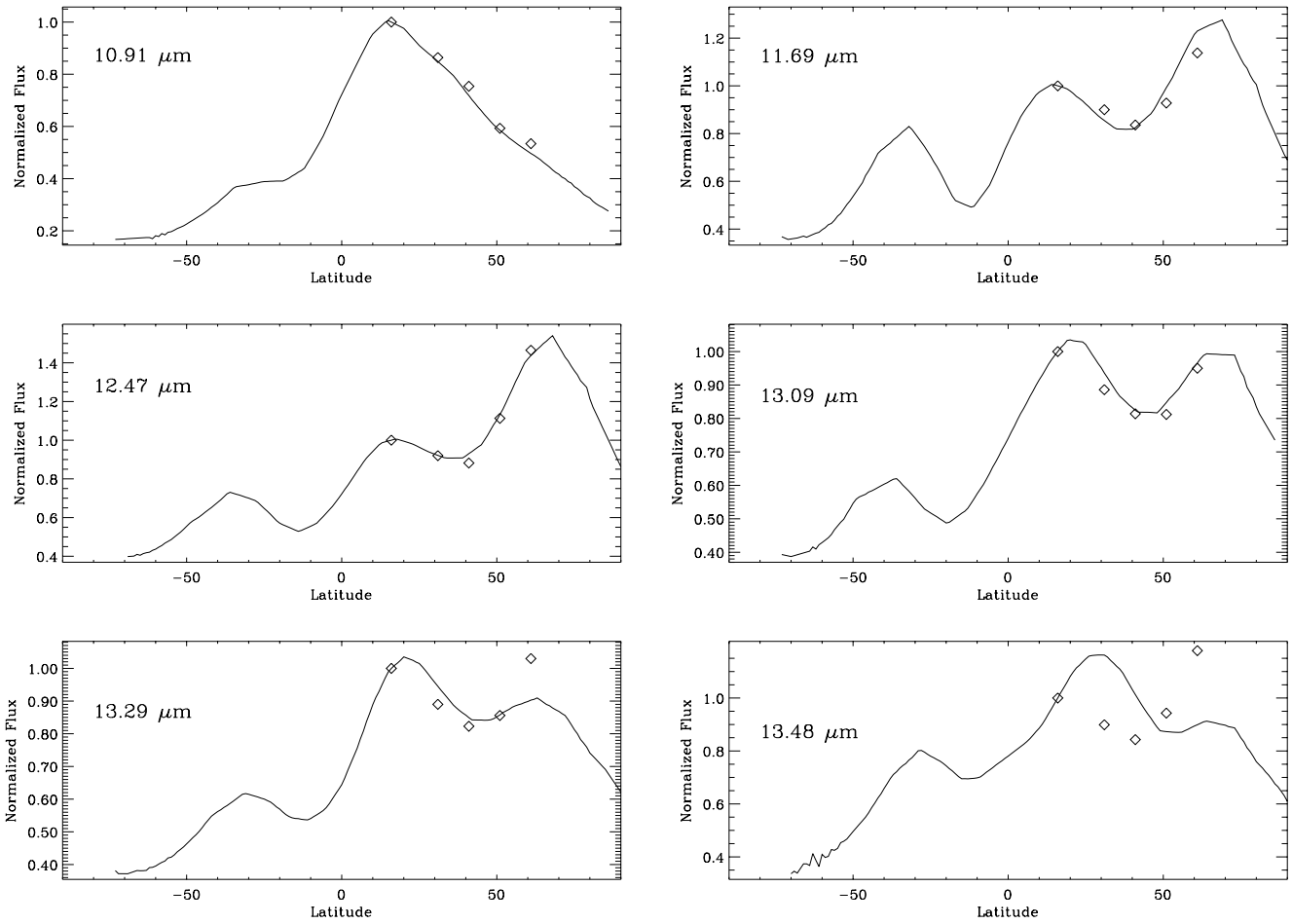

Fig. 6. The results of the radiative transfer model compared to the flux observed on the central meridian. We show here the results for the first hypothesis: constant ethane and acetylene abundances and variable thermal profile. The flux is represented as a normalized flux: we divide the flux at each latitude by the flux at 17°N. In order to increase the signal-to-noise ratio, we average the flux over 5° in longitude.

in the atmosphere of Saturn. The following discussion only focus on the NPE. Gezari et al. (1989) have made 3 images of Saturn at 7.8, 11.6 and 12.4 μm. On each of their images they saw the NPE. Concerning the images at 11.6 and 12.4 μm, their observations are consistent with our two assumptions since the wavelengths used are almost the same as ours, i.e. sensitive to the ethane emission. As regards the 7.8 μm image, it is sensitive to the methane emission band. So the NPE seen on this image implies either an enhancement in the methane abundance or a higher stratospheric temperature (the contribution function at 7.8 μm peaks in the lower stratosphere). Due to the photochemical origin of ethane and acetylene, their abundances depend directly on that of methane, and a greater methane abundance would produce a greater abundance of ethane and acetylene, which would explain the enhanced flux at 11.6 and 12.4 μm. A problem arises with the increased methane abundance. Indeed, the methane mole fraction is constant in the deep atmosphere of the giant planets and it would be difficult to explain an enhanced methane mole fraction. It is thus likely that the observed structure at 7.8 μm is caused by an enhanced temperature and not by a larger methane abundance.

Tokunaga et al. (1978) studied Saturn's infrared emission using north-south scans at 17.8, 19.7 and 22.7 μm obtained in 1975 and 1977. Their observations were made when Saturn presented a geometry opposite to the one we have: the tilt of the south pole of Saturn towards the sun was about 15°, whereas during our observations, Saturn presents the same tilt angle, with the north pole being towards the sun. Furthermore we observed Saturn in 1992, 15 and 17 years after the observations of Tokunaga et al., which corresponds to half a period of Saturn's revolution around the Sun. Therefore we have symetrical observation conditions which would imply that we should observe the same features as Tokunaga et al. (1978), but now for the north pole. Bézard & Gautier (1985), who computed the seasonal cycle of Saturn's stratosphere, showed that, at 5 mbar, the temperature of the north pole in 1992 should be nearly the same as that of the south pole in 1975-1977. The thermal inversion in Saturn's atmosphere is located around 60 mbar, below the 5 mbar level, but it is likely that the thermal variation calculated by Bézard & Gautier extends to levels around the thermal inversion. Tokunaga et al. (1978) observations revealed the presence of a strong enhanced emission at the south pole at a wavelength range (around 20μm)

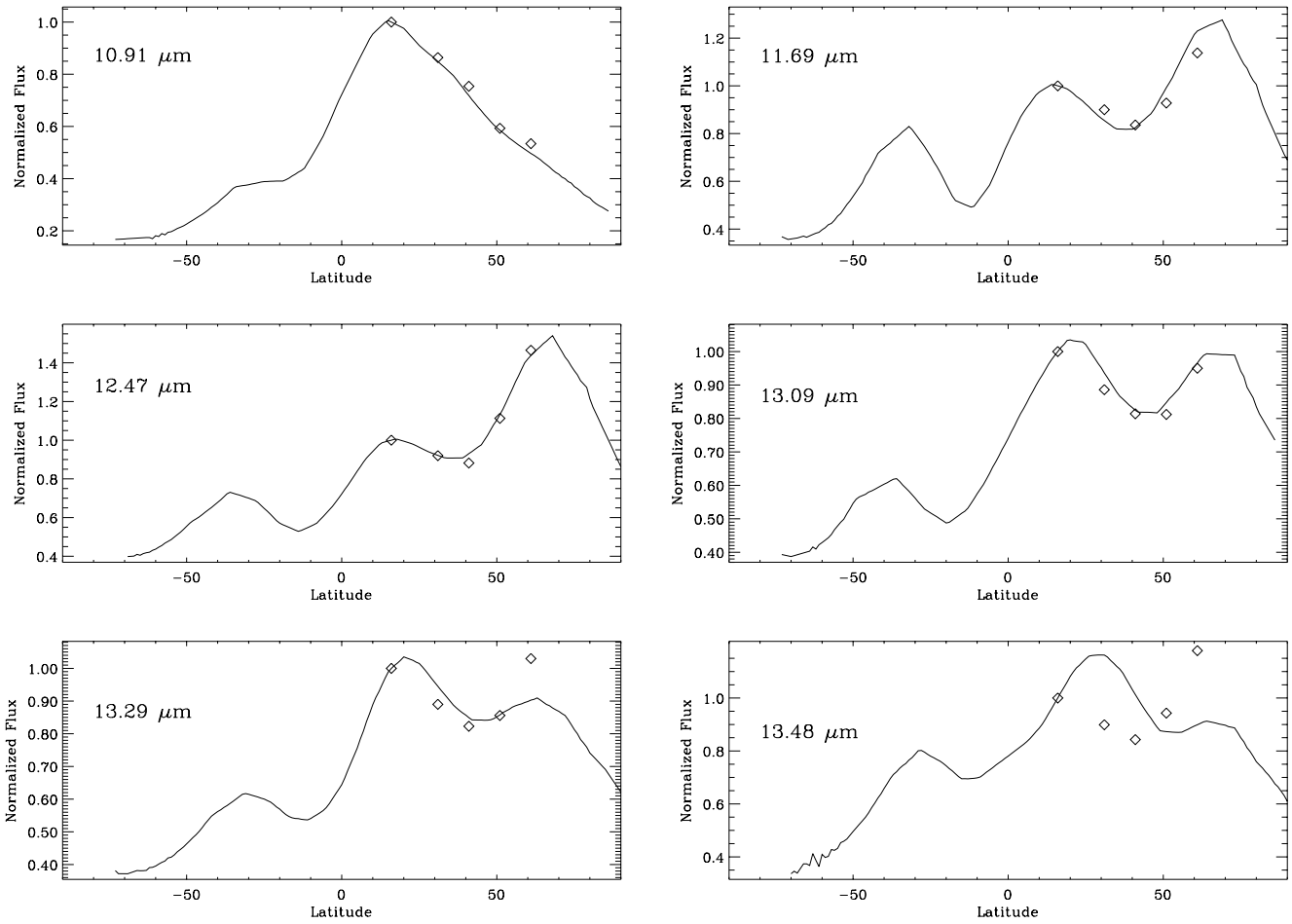

Fig. 7. The results of the radiative transfer model compared to the flux observed on the central meridian. We show here the results for the second hypothesis: variable ethane and acetylene abundances and constant thermal profile shape. The flux is represented as a normalized flux: we divide the flux at each latitude by the flux at 17°N. As in Fig. 6 we average the flux over 5° in longitude.

which is not sensitive to hydrocarbon emissions. Moreover, simultaneous equatorial scans showed that the limb brightening at the equator is smaller (Caldwell et al. 1978). This implies, as reported by Tokunaga et al. (1978), that the temperature of the atmospheric levels around the thermal inversion is hotter at the south pole. From the above considerations, it is likely that the levels around the tropopause at the north pole should show a higher temperature at the epoch of our observations. We did not observe Saturn in the 20μm window, but the images at 10.91 μm also probe the thermal continuum. The interesting point is that at 10.91 μm, we do not see any polar brightening. The maximum of the contribution function at 17.8 μm is located just around 100 mbar and near 500 mbar at 10.91 μm. In order to see if a hotter tropopause could produce a brightening at 17.8 μm and could be invisible at 10.91 μm, we calculate the emission at these two wavelengths with two different thermal profiles, the only difference being the hotter tropopause (+3K). For emission angle corresponding to high latitudes, we find an enhancement of about 20% at 17.8 μm, but a similar 10.91 μm flux in the two cases. Therefore, the absence of a polar emission at 10.91 μm does not imply the abscence of a polar emission at 17.8 μm. With all this information, we can postulate that the seasonal evolution of insolation produces thermal effects, the insolated pole being hotter, and these effects concern only the upper troposphere (above 200-300 mbar) and the stratosphere. This agrees quite well with the results of Conrath and Pirraglia (1983) who derived the latitudinal variation of the temperature at three pressure levels, 730, 290 and 150 mbar. The thermal asymmetry between the northern and southern hemispheres, which is an effect of the seasonal varying insolation, is clear only at 150 mbar but not at 730 mbar, in agreement with our results. Moreover, from calculations with radiative-dynamical models, Conrath et al. (1990) and Barnet et al. (1992) showed that, at north summer solstice, levels below 300 mbars have a constant temperature over all latitudes (Fig. 9b of Conrath et al. (1990) and Fig. 6 of Barnet et al. (1992)), the upper levels being sensitive to the seasonal variation. And the calculated structure of the atmosphere seems to be in good agreement with the observed one. Indeed, we have already noticed that these calculations lead to a good agreement with the observations of Gezari et al. (1989) which were obtained near north summer solstice. Our observations were conducted when the solar longitude of Sat-

urn was about 145°, during northern summer. Due to the phase lag between the insolation and the thermal response of the atmosphere (Conrath & Pirraglia,1983, Conrath et al.1990), the northern hemisphere is still warming at the time of our observations, and these two radiative-dynamical models are in good agreement with the global structure of the atmosphere derived from our observations. Nevertheless, the precise calculation of the structure of the atmosphere at the precise time of the observations would be necessary to determine exactely the order of magnitude of the latitudinal temperature variations, in order to compare with our results (models should find a variation of the order of 10K between 15°N and 60°N). Furthermore, the NEB, which we associate with the temperature enhancement between 10 and 20°N observed by Voyager/IRIS (Conrath & Pirraglia, 1983) seems to be difficult to reproduce with these models, and further improvements of such models are necessary to provide a better understanding this particular feature and the thermal structure of Saturn's atmosphere.

Finally, we conclude that the hypothesis of a hydrocarbon abundance enhancement is not necessary. Nevertheless, it is likely that such variations occur but probably not with the order of magnitude found here. The enhanced abundances found here are more likely the upper limits of ethane and acetylene abundances. The processes which may be responsible for this enhancement still remain to be identified. For instance, one important parameter for the photochemistry is the temperature profile since chemical reactions are temperature-dependent. Therefore, the hydrocarbon abundances should vary with latitude as the temperature profile varies. Furthermore, processes involving energetic particles could produce significant effects which could lead to a variability of hydrocarbon abundances (as suggested by Kostiuk et al. 1987, in the case of Jupiter).

7. Conclusion

The present study of Saturn's atmosphere through thermal infrared imaging has explored two possible ways in interpreting the observed infrared structure of Saturn's atmosphere. The first assumption is the classical one: the tilt of Saturn's spin axis leads to a strong seasonal cycle which produces a thermal asymmetry, the insolated pole being hotter. From a comparison with a radiative transfer code, we showed that, with this hypothesis, the tropospheric temperature is nearly constant with latitude (it decreases by 3K from the equator to 60°N), while the stratospheric temperature is highly variable (the stratospheric temperature at 60°N is about 12K higher than at 40°N).

The second assumption explored the possibility of a variation in ethane and acetylene abundances. From our images, we showed that enhanced ethane and acetylene abundances can explain the features observed with a specific thermal profile. However when we consider previous infared observations in the 20 μm window (Tokunaga et al. 1978), it is likely that this hypothesis is not valid. We conclude that Saturn's atmosphere shows a thermal variation constrained by the solar insolation. This variation affects mainly the upper atmosphere above 200-300 mbar. A next step could be to study the influence of such a variation on other atmospheric parameters, such as compound abundances or cloud structure.

References

Atreya S.K., 1986, Atmospheres and Ionospheres of the Outer Planets and their Satellites, Springer-Verlag
Barnet C.D., Beebe R.F., Conrath, B.J., 1992, Icarus 98, 94
Bézard B., Gautier D., 1985, Icarus 61, 296
Bézard B., Gautier D., Conrath B., 1984, Icarus 60, 274
Billebaud F., Drossart P., Vauglin I., et al., 1995, Geophys. Res. Lett.22, 1777
Borysow J., Trafton L., Frommhold L., et al., 1985, ApJ296, 644
Caldwell J., Gillett F.C., Nolt, I.G., et al., 1978, Icarus 35, 308
Conrath B.J., Pirraglia, J.A., 1983, Icarus 53, 286
Conrath B.J., Gierasch P.J., Leroy S.S., 1990, Icarus 83, 255
Courtin R., Gautier D., Marten A., et al., 1984, ApJ287, 899
de Graauw T., Feuchtgruber H., Bezard B., et al., 1997, A&A321, L13
Gezari D.Y., Mumma M.J., Espenak F., et al., 1989, Nature342, 777
Gillett F.C., Orton G.S., 1975, ApJ195, L47
Gladstone G.R., Allen, M., Yung Y.L., 1996, Icarus 119, 1
Hanel R., Conrath B.J., Flasar F., et al., 1982, Science 215, 544
Hubbard W. B., Porco C.C., Hunten D.M., et al., 1997, Icarus 130, 404
Jacquinet-Husson N., Arie E., Ballard J., et al., 1998, J. Quant. Spec. Radiat. Transf. 59, 511
Kostiuk T., Espenak F., Mumma M.J., et al., 1987, Icarus 72, 394
Lindal G.F., Sweetnam D.N., Eshleman V.R., 1985, AJ 90, 1136
Moses J.I., Bézard B., Lellouch E., et al., 1999, Icarus (submitted)
Ollivier J.L., Dobrijévic M., Parisot, J.P., 2000a, Planet. Space Sci. (accepted)
Ollivier J.L., Dobrijévic M., Parisot J.P., 2000b, (in preparation)
Olnon F.M., Raimond E., Neugebauer G. et al., 1986, A&AS 65, 607
Rieke G.H., 1975, Icarus 26, 37
Roos-Serote M., Drossart P., Encrenaz T., et al., 1998, J. Geophys. Rev. 103, 23023
Strobel D.F., 1983, Int. Rev. Phys. Chem. 3, 145
Tokunaga A.T., Caldwell J., Gillett F.C., et al., 1978, Icarus 36, 216
Vauglin I., Merlin P., Sibille F., 1999, User's Manual for the 10 micron camera C10mu, available at http://www-obs.univ-lyon1.fr/ir